

Unsupervised Hyperspectral Mixed Noise Removal Via Spatial-Spectral Constrained Deep Image Prior

Yi-Si Luo, Xi-Le Zhao, *Member, IEEE*, Tai-Xiang Jiang, *Member, IEEE*, Yu-Bang Zheng, *Student Member, IEEE*, and Yi Chang, *Member, IEEE*

Abstract—Recently, convolutional neural network (CNN)-based methods are proposed for hyperspectral images (HSIs) denoising. Among them, unsupervised methods such as the deep image prior (DIP) have received much attention because these methods do not require any training data. However, DIP suffers from the semi-convergence behavior, i.e., the iteration of DIP needs to terminate by referring to the ground-truth image at the optimal iteration point. In this paper, we propose the spatial-spectral constrained deep image prior (S2DIP) for HSI mixed noise removal. Specifically, we incorporate DIP with a spatial-spectral total variation (SSTV) term to fully preserve the spatial-spectral local smoothness of the HSI and an ℓ_1 -norm term to capture the complex sparse noise. The proposed S2DIP jointly leverages the expressive power brought from the deep CNN without any training data and exploits the HSI and noise structures via hand-crafted priors. Thus, our method avoids the semi-convergence behavior, showing higher stabilities than DIP. Meanwhile, our method largely enhances the HSI denoising ability of DIP. To tackle the proposed denoising model, we develop an alternating direction multiplier method algorithm. Extensive experiments demonstrate that the proposed S2DIP outperforms optimization-based and supervised CNN-based state-of-the-art HSI denoising methods.

Index Terms—Hyperspectral image, Denoising, Convolutional neural networks, Unsupervised, Spatial-spectral.

I. INTRODUCTION

HYPERSPECTRAL images (HSIs) contain abundant spatial and spectral information and thus can be utilized into various applications, such as object detection [2], [3], classification [4]–[6], and so on. Due to the imaging environment, HSIs are inevitably corrupted by mixed noise. The complex noise seriously affects subsequent applications as well as visual qualities. Thus, HSI denoising is considered an essential technique in hyperspectral imaging.

Earlier HSI denoising methods are dominated by model-based techniques [7]–[10], such as total variation (TV)-based

This research is supported by NSFC (No. 61876203, 61772003), the Applied Basic Research Project of Sichuan Province (No. 2021YJ0107), the Key Project of Applied Basic Research in Sichuan Province (No. 2020YJ0216), and National Key Research and Development Program of China (No. 2020YFA0714001).

Y.-S. Luo, X.-L. Zhao, and Y.-B. Zheng are with the Research Center for Image and Vision Computing, School of Mathematical Sciences, University of Electronic Science and Technology of China, Chengdu, P.R.China (e-mail: yisiluo1221@foxmail.com; xlzhao122003@163.com; zhengyubang@163.com).

T.-X. Jiang is with the FinTech Innovation Center, the Financial Intelligence and Financial Engineering Research Key Laboratory of Sichuan Province, School of Economic Information Engineering, Southwestern University of Finance and Economics, Chengdu, P.R.China (e-mail: taixiangjiang@gmail.com).

Y. Chang is with the Artificial Intelligence Research Center, Peng Cheng Laboratory, Shenzhen, P.R.China (e-mail: yichang@hust.edu.cn).

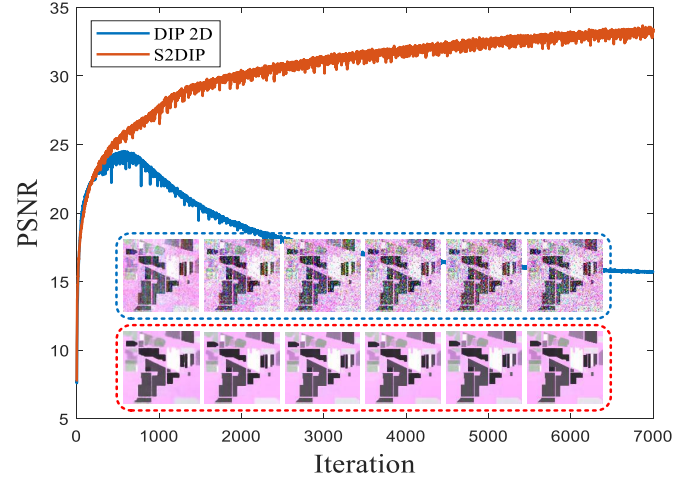


Fig. 1. The history of PSNR values of the denoising results by DIP 2D [1] and S2DIP with respect to the iterations. Compared to DIP 2D, S2DIP is more stable and achieves better results for HSI mixed noise removal.

methods [11]–[14], sparsity-based methods [15], [16], non-local-based methods [17], dictionary learning-based methods [25], [26], and matrix/tensor low-rankness-based methods [18]–[24]. These methods exploit the intrinsic structure of HSIs via optimization-based models to deal with the HSI denoising. With meticulously selected hand-crafted priors, recent model-based methods [18], [20], [27] have achieved state-of-the-art performance. These state-of-the-art methods mainly consider the matrix/tensor low-rankness and form the HSI denoising [28], [29] as a low-rank matrix/tensor recovery problem. Other hand-crafted priors such as TV [30], [31] can be combined in such low-rank model and algorithms like alternating direction multiplier method (ADMM) can be utilized to address the denoising model.

Inspired by the success of deep learning in inverse problems in imaging [32]–[35], convolutional neural network (CNN)-based methods [36]–[41] have emerged for HSI denoising in last few years. Generally, most of the CNN-based methods learn the noisy-to-denoising mapping driven by abundant training data [37], [39], which leads to great performance for HSI denoising on specific datasets. Nevertheless, the effectiveness of supervised CNN-based methods critically depends on the diversity and quantity of training data. However, hyperspectral data is limited and the real noise of HSIs is complex. Thus, it is difficult to guarantee high-quality denoising results under the realist complex noise scenario of HSIs, where the underlying assumption is not held in the training data.

Recently, an unsupervised image restoration method deep image prior (DIP) [42] was proposed. The DIP employs the CNN and optimizes its learnable parameters by targeting the observed image as the network output with a randomly given input, demonstrating that the CNN itself can represent a well-reconstructed image by the iterative process without any training data. Afterward, Sidorov et al. extended the DIP into HSI restoration [1], which yields decent performance on HSI denoising, inpainting, and super-resolution.

However, DIP suffers from the semi-convergence behavior, which refers to the behavior of an iterative method that the PSNR value begins to increase at early iterations and, after a certain “optimal” iteration, the PSNR value begins to decrease, see Fig. 1. Hence, the iteration needs to terminate by referring to the ground-truth image at the point of the highest PSNR value, before fitting the noise. Meanwhile, DIP has relatively weak performance for HSI denoising compared with existing state-of-the-art methods [18], [20], [39]. We attribute these deficiencies of DIP to two aspects. First, DIP lacks specific characterization on HSI intrinsic structures. HSIs have unique spatial-spectral structures, which require specific prior terms to characterize. Second, DIP lacks robust noise modeling. In real applications, the noise of HSI is very complex and various. Only considering Gaussian noise and neglect other types of noise is not enough to completely remove the complex noise in HSI.

In this paper, we propose the spatial-spectral constrained deep image prior (S2DIP) for HSI mixed noise removal. We combine DIP with prior information on both HSI and hyperspectral noise. Specifically, we employ a spatial-spectral total variation (SSTV) term to explore the spatial-spectral local smoothness of HSIs and an ℓ_1 -norm term to capture the sparse noise for mixed noise removal. To tackle the proposed denoising model, we develop an ADMM algorithm. Meanwhile, we elaborately design an automatic stopping criterion to verify the stability of S2DIP. The DIP, HSI prior, and noise prior are complementary to each other and are organically combined to benefit each other. The proposed S2DIP could favorably address the semi-convergence behavior of DIP and largely improves the effectiveness and robustness for HSI mixed noise removal.

Compared with traditional optimization-based HSI denoising methods, the proposed S2DIP capitalizes the expressive power from the CNN and holds higher model representation ability. Compared with supervised CNN-based methods, the proposed S2DIP does not need training data and has a better generalization ability for diverse HSI data with various complex noise.

We summarize the contributions of this paper as:

- We propose the S2DIP for HSI mixed noise removal. Specifically, we incorporate DIP with an SSTV term to fully explore the spatial-spectral local smooth prior of the underlying HSI and an ℓ_1 -norm sparse term to capture the sparse noise. Our method avoids the semi-convergence behavior and is more stable than DIP. Meanwhile, with the comprehensive consideration of the deep prior, HSI prior, and sparse noise prior, the proposed S2DIP could achieve promising HSI denoising results.

- To tackle the proposed denoising model, we develop an efficient ADMM algorithm. In company, we elaborately design an automatic stopping criterion without referring to the ground-truth image.
- Extensive experiments on HSIs, MSIs, and videos validate the effectiveness and generalization ability of the proposed method. The proposed method outperforms optimization-based and CNN-based state-of-the-art methods. Moreover, HSI classification results after the denoising are reported to validate the effectiveness of the proposed method.

The rest of this paper is organized as follows. In Sec. II, we introduce some related work. In Sec. III, we introduce the proposed S2DIP. In Sec. IV, we carry out the experimental results. Sec. V provides some discussions. Finally, Sec. VI concludes this paper.

II. RELATED WORK

A. Model-Based Methods for HSI Denoising

Traditional HSI denoising methods are dominated by model-based methods. These methods, including but not limited to TV-based methods [11]–[14], [43]–[45], sparsity-based methods [15], [16], [29], and matrix/tensor low-rankness-based methods [18]–[24], [28], [46], consider the HSI prior information and establish optimization model and corresponding algorithms for denoising. For instance, Zhang et al. [18] vectorized each band of the HSI as a column and unfolds them as a matrix, and then considered the low-rank property on the unfolded matrix. Wang et al. [20] utilized the tensor decomposition, which delivered the global tensor low-rankness. The TV regularization was considered along with the tensor decomposition. Such methods achieve state-of-the-art performance due to the comprehensive consideration of the HSI prior information.

B. CNN-Based Methods for HSI Denoising

In recent years, the CNN-based approaches for HSI denoising [37]–[41], [47], [48] have emerged and present state-of-the-art performance. For instance, Yuan et al. [39] employed the deep residual CNN to conduct HSI denoising. Dong et al. [37] utilized the deep 3D encoder-decoder network for HSI denoising. Cao et al. [48] used the deep spatial-spectral global reasoning network for HSI denoising. The core concept of these methods is to train a CNN with abundant pairs of training data $\{\mathcal{Y}, \mathcal{X}\}$, where \mathcal{Y} denotes the dataset of noisy HSIs and \mathcal{X} denotes the dataset of corresponding clean HSIs. The training process could be described as

$$\min_{\Theta} \mathcal{L}(f_{\Theta}(\mathcal{Y}), \mathcal{X}), \quad (1)$$

where $f_{\Theta}(\cdot)$ denotes a CNN with learnable parameters Θ , and \mathcal{L} is the loss function. The well-trained CNN can be viewed as a noisy-to-denoising mapping. Due to the powerful nonlinear modeling ability of the deep CNN, supervised methods have achieved promising results on specific datasets and specific noisy types.

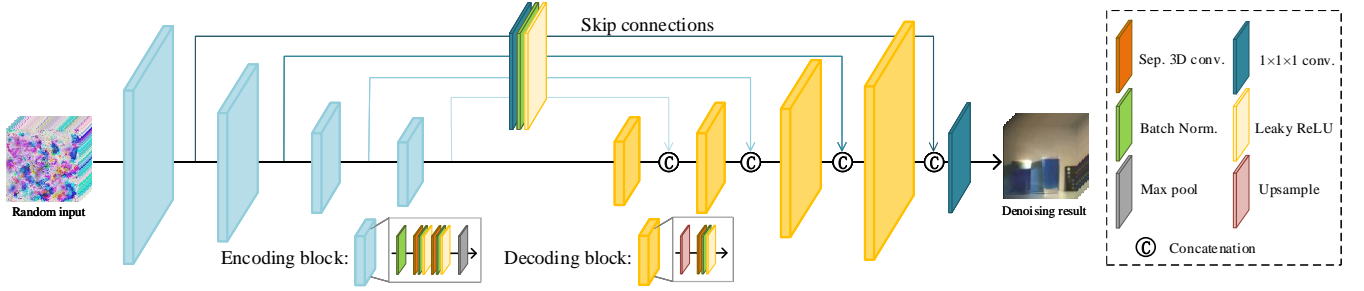


Fig. 2. The network structure used in this work. The separable 3D convolution-driven encoder-decoder network aims at preferably representing the spatial and spectral features under the unsupervised condition.

C. Deep Image Prior

Recently, Ulyanov et al. [42] proposed an unsupervised deep learning-based image restoration technique, named deep image prior. The DIP uses CNN to conduct image restoration without any training process. By targeting the degraded image as the network output with randomly generated network input, the CNN could remove the Gaussian noise from the degraded image with appropriate iteration steps. Afterward, Sidorov et al. [1] extended DIP into HSI restoration.

Similar to the supervised methods, the optimization process of DIP for HSI [1] restoration is formulated as

$$\min_{\Theta} \frac{1}{N} \|f_{\Theta}(\mathcal{Z}) - \mathcal{Y}\|_{\ell_2}^2, \quad (2)$$

where $\mathcal{Z} \in \mathbb{R}^{H \times W \times B}$ denotes the randomly generated network input and \mathcal{Y} denotes the noisy HSI. The mean square error (MSE) is adopted as the loss function, where $N = H \times W \times B$ denotes the number of total pixels. The gradient descent algorithm is adopted to iteratively optimize the CNN. Obviously, the optimization process will finally converge to a noisy HSI $f_{\Theta}(\mathcal{Z})$, which is almost structurally identical with the observation \mathcal{Y} . However, it has been discovered that the network will firstly fit the signal part of the observation, and then fit the noisy part [42]. Thus, the denoising of \mathcal{Y} can be achieved by stopping the iteration at appropriate steps before the network fitting noise, and the denoising result is obtained by $\mathcal{X} = f_{\Theta^*}(\mathcal{Z})$ with Θ^* denotes the network parameters after appropriate iterations. This is also a key limitation of DIP, where the denoising iterative process must be stopped by referring to the ground-truth image at the optimal point, see Fig. 1 for an example of DIP for HSI denoising. We refer to this limitation as semi-convergence. In this paper, we avoid this issue by combining DIP with spatial-spectral priors of HSI and the sparse prior of hyperspectral noise.

III. THE PROPOSED S2DIP

This section introduces the proposed S2DIP. First, we introduce the degradation model of hyperspectral mixed noise. Then, we give the network structure of the proposed method and form the optimization model for HSI denoising. To address the proposed model, We develop an ADMM algorithm. Finally, we propose an automatic stopping criterion to be used for verifying the stability of S2DIP, which addresses the semi-convergence of DIP.

A. Degradation Model

The noise in HSI is complex and various. Only considering Gaussian noise [1] is hard to comprehensively remove the complex noise. This motivates us to improve the generalization ability of DIP by considering more robust noise modeling. In this work, we consider the noisy HSI as an addition of the clean HSI, the Gaussian noise, and the sparse structural noise [13], [20]. The degradation process can be formulated as

$$\mathcal{Y} = \mathcal{X} + \mathcal{N} + \mathcal{S}, \quad (3)$$

where $\mathcal{Y} \in \mathbb{R}^{H \times W \times B}$ denotes the observed noisy HSI, $\mathcal{X} \in \mathbb{R}^{H \times W \times B}$ denotes the underlying clean HSI, $\mathcal{N} \in \mathbb{R}^{H \times W \times B}$ denotes the Gaussian noise, and $\mathcal{S} \in \mathbb{R}^{H \times W \times B}$ denotes the sparse structural noise. Our method will use the deep prior of CNN to generate \mathcal{X} and fully consider the spatial-spectral prior information of \mathcal{X} and the sparsity of \mathcal{S} for mixed noise removal.

B. Network Architecture of S2DIP

We employ a U-Net with skip connections for HSI denoising [1], [42], see Fig. 2. The input data is the random noise, which goes through the encoder and progressively outcomes embedded three-dimensional features. The embedded features go through the decoder to reconstruct the clean HSI.

In [1], the author tried both 2D and 3D convolution in the U-Net for HSI denoising. However, it appears that the performance of 3D convolution is inferior to that of 2D convolution. In this paper, we use the separable 3D convolution [49], which is shown to be more capable to encode the HSI than 3D convolution [37]. The separable 3D convolution represents the spatial and spectral information using 2D and 1D kernels respectively so that better representation of the HSI can be obtained, see more details in [37]. Here, we employ four layers in both encoding and decoding stages. We denote the proposed separable 3D U-Net by $f_{\Theta}(\cdot)$ with Θ refers to the learnable parameters. We randomly initialize the parameters of the network. The network parameters are iteratively and unsupervisedly updated (see Sec. III-D and Algorithm 1). Except for the observed HSI, no extra training data is needed.

C. Optimization Model of S2DIP

Spatial-spectral constraint: The optimization model of DIP (2) aims at fitting the noisy HSI while the noise could

be removed using the ‘‘deep prior’’ of CNN. However, it is unavoidable for DIP that the CNN will eventually fit the noise, which causes semi-convergence. To address this issue, we propose to use the SSTV regularization to fully preserve the spatial-spectral local smoothness of the network output so that spatial-spectral consistency can be ensured. The SSTV term is expected to address the semi-convergence and simultaneously improve the denoising performance.

Formally, for a three-way tensor $\mathcal{X} \in \mathbb{R}^{H \times W \times B}$, its difference tensors $\nabla_x \mathcal{X} \in \mathbb{R}^{(H-1) \times W \times B}$, $\nabla_y \mathcal{X} \in \mathbb{R}^{H \times (W-1) \times B}$, and $\nabla_z \mathcal{X} \in \mathbb{R}^{H \times W \times (B-1)}$ are defined as

$$\begin{cases} \nabla_x \mathcal{X}(i, j, k) = \mathcal{X}(i+1, j, k) - \mathcal{X}(i, j, k) \\ \nabla_y \mathcal{X}(i, j, k) = \mathcal{X}(i, j+1, k) - \mathcal{X}(i, j, k) \\ \nabla_z \mathcal{X}(i, j, k) = \mathcal{X}(i, j, k+1) - \mathcal{X}(i, j, k), \end{cases} \quad (4)$$

where $\mathcal{X}(i, j, k)$ denotes the (i, j, k) -th element of \mathcal{X} , and ∇_x , ∇_y , and ∇_z denote the finite difference operators on the vertical direction, horizontal direction, and spectral direction, respectively. The TV of \mathcal{X} is given by

$$\|\mathcal{X}\|_{\text{TV}} = \|\nabla_x \mathcal{X}\|_{\ell_1} + \|\nabla_y \mathcal{X}\|_{\ell_1}. \quad (5)$$

Further considering the spatial-spectral local smoothness, the SSTV [12] of \mathcal{X} is given by

$$\|\mathcal{X}\|_{\text{SSTV}} = \|\nabla_x(\nabla_z \mathcal{X})\|_{\ell_1} + \|\nabla_y(\nabla_z \mathcal{X})\|_{\ell_1}. \quad (6)$$

The TV considers the spatial local smoothness and SSTV considers the spatial-spectral local smoothness. To faithfully utilize both of their properties, we introduce both TV and SSTV in the optimization model of DIP to explore the spatial and spatial-spectral local smooth prior of HSIs under unsupervised conditions.

Sparse noise modeling: The DIP model (2) only considers the Gaussian noise. In real applications, the noise of HSI is complex and various. In this paper, we further consider the sparse noise to improve the generalization ability of DIP for more robust denoising. The sparse noise contains impulse noise and stripes that are commonly existing in HSIs. We consider minimizing the ℓ_1 -norm of \mathcal{S} to enforce the sparsity on \mathcal{S} so that the sparse noise can be faithfully separated from the clean HSI.

Based on the analysis of spatial-spectral constraints and sparse noise modeling, the proposed optimization model for HSI mixed noise removal is formulated as

$$\begin{aligned} \min_{\Theta, \mathcal{S}} \|\mathcal{Y} - \mathcal{X} - \mathcal{S}\|_F^2 + \alpha_1 \|\mathcal{X}\|_{\text{TV}} + \alpha_2 \|\mathcal{X}\|_{\text{SSTV}} \\ + \alpha_3 \|\mathcal{S}\|_{\ell_1} \\ \text{s.t. } \mathcal{X} = f_{\Theta}(\mathcal{Z}), \end{aligned} \quad (7)$$

where $\alpha_i (i = 1, 2, 3)$ are trade-off parameters. Here, $\|\mathcal{X}\|_{\text{TV}}$ and $\|\mathcal{X}\|_{\text{SSTV}}$ are the TV and SSTV regularizations, respectively. $\|\mathcal{S}\|_{\ell_1}$ is the ℓ_1 -norm of the sparse noise. $\|\mathcal{Y} - \mathcal{X} - \mathcal{S}\|_F^2$ is the fidelity term. The CNN $f_{\Theta}(\cdot)$ with random input \mathcal{Z} is used to model the clean HSI \mathcal{X} .

In our model, the deep prior, HSI prior, and sparse noise prior are complementary to each other and are organically combined to remove the mixed noise in HSI.

D. Algorithm

To tackle the proposed model (7), we develop an efficient ADMM algorithm. By introducing four auxiliary variables $\mathcal{V}_i (i = 1, 2, 3, 4)$, we can formulate (7) as

$$\begin{aligned} \min_{\Theta, \mathcal{S}} \|\mathcal{Y} - f_{\Theta}(\mathcal{Z}) - \mathcal{S}\|_F^2 + \alpha_1 \|\mathcal{V}_1\|_{\ell_1} + \alpha_1 \|\mathcal{V}_2\|_{\ell_1} \\ + \alpha_2 \|\mathcal{V}_3\|_{\ell_1} + \alpha_2 \|\mathcal{V}_4\|_{\ell_1} + \alpha_3 \|\mathcal{S}\|_{\ell_1} \\ \text{s.t. } \mathcal{V}_1 = \nabla_x(f_{\Theta}(\mathcal{Z})), \mathcal{V}_2 = \nabla_y(f_{\Theta}(\mathcal{Z})), \\ \mathcal{V}_3 = \nabla_x \nabla_z(f_{\Theta}(\mathcal{Z})), \mathcal{V}_4 = \nabla_y \nabla_z(f_{\Theta}(\mathcal{Z})). \end{aligned} \quad (8)$$

The augmented Lagrangian function of (8) is

$$\begin{aligned} \mathcal{L}_{\mu}(\Theta, \mathcal{S}, \mathcal{V}_i, \Lambda_i) \\ = \|\mathcal{Y} - f_{\Theta}(\mathcal{Z}) - \mathcal{S}\|_F^2 + \alpha_1 \|\mathcal{V}_1\|_{\ell_1} + \alpha_1 \|\mathcal{V}_2\|_{\ell_1} \\ + \alpha_2 \|\mathcal{V}_3\|_{\ell_1} + \alpha_2 \|\mathcal{V}_4\|_{\ell_1} + \frac{\mu}{2} \|\nabla_x(f_{\Theta}(\mathcal{Z})) - \mathcal{V}_1\|_F^2 \\ + \frac{\mu}{2} \|\nabla_y(f_{\Theta}(\mathcal{Z})) - \mathcal{V}_2\|_F^2 + \frac{\mu}{2} \|\nabla_x \nabla_z(f_{\Theta}(\mathcal{Z})) - \mathcal{V}_3\|_F^2 \\ + \frac{\mu}{2} \|\nabla_y \nabla_z(f_{\Theta}(\mathcal{Z})) - \mathcal{V}_4\|_F^2 + \alpha_3 \|\mathcal{S}\|_{\ell_1} \\ + \langle \Lambda_1, \nabla_x(f_{\Theta}(\mathcal{Z})) - \mathcal{V}_1 \rangle + \langle \Lambda_2, \nabla_y(f_{\Theta}(\mathcal{Z})) - \mathcal{V}_2 \rangle \\ + \langle \Lambda_3, \nabla_x \nabla_z(f_{\Theta}(\mathcal{Z})) - \mathcal{V}_3 \rangle \\ + \langle \Lambda_4, \nabla_y \nabla_z(f_{\Theta}(\mathcal{Z})) - \mathcal{V}_4 \rangle, \end{aligned} \quad (9)$$

where μ is the penalty parameter and $\Lambda_i (i = 1, 2, 3, 4)$ are the multipliers. Using the ADMM, the problem can be divided into the following sub-problems.

\mathcal{V} Sub-problems: The $\mathcal{V}_i (i = 1, 2, 3, 4)$ sub-problems are

$$\begin{cases} \min_{\mathcal{V}_1} \frac{\mu}{2} \left\| \nabla_x(f_{\Theta^t}(\mathcal{Z})) + \frac{\Lambda_1^t}{\mu} - \mathcal{V}_1 \right\|_F^2 + \alpha_1 \|\mathcal{V}_1\|_{\ell_1} \\ \min_{\mathcal{V}_2} \frac{\mu}{2} \left\| \nabla_y(f_{\Theta^t}(\mathcal{Z})) + \frac{\Lambda_2^t}{\mu} - \mathcal{V}_2 \right\|_F^2 + \alpha_1 \|\mathcal{V}_2\|_{\ell_1} \\ \min_{\mathcal{V}_3} \frac{\mu}{2} \left\| \nabla_x \nabla_z(f_{\Theta^t}(\mathcal{Z})) + \frac{\Lambda_3^t}{\mu} - \mathcal{V}_3 \right\|_F^2 + \alpha_2 \|\mathcal{V}_3\|_{\ell_1} \\ \min_{\mathcal{V}_4} \frac{\mu}{2} \left\| \nabla_y \nabla_z(f_{\Theta^t}(\mathcal{Z})) + \frac{\Lambda_4^t}{\mu} - \mathcal{V}_4 \right\|_F^2 + \alpha_2 \|\mathcal{V}_4\|_{\ell_1}, \end{cases} \quad (10)$$

which can be exactly solved by

$$\begin{cases} \mathcal{V}_1^{t+1} = \text{Soft}_{\frac{\alpha_1}{\mu}} \left(\nabla_x(f_{\Theta^t}(\mathcal{Z})) + \frac{\Lambda_1^t}{\mu} \right) \\ \mathcal{V}_2^{t+1} = \text{Soft}_{\frac{\alpha_1}{\mu}} \left(\nabla_y(f_{\Theta^t}(\mathcal{Z})) + \frac{\Lambda_2^t}{\mu} \right) \\ \mathcal{V}_3^{t+1} = \text{Soft}_{\frac{\alpha_2}{\mu}} \left(\nabla_x \nabla_z(f_{\Theta^t}(\mathcal{Z})) + \frac{\Lambda_3^t}{\mu} \right) \\ \mathcal{V}_4^{t+1} = \text{Soft}_{\frac{\alpha_2}{\mu}} \left(\nabla_y \nabla_z(f_{\Theta^t}(\mathcal{Z})) + \frac{\Lambda_4^t}{\mu} \right), \end{cases} \quad (11)$$

where $\text{Soft}_v(\cdot)$ is the soft-thresholding operator defined as

$$\text{Soft}_v(\mathcal{X})(i, j, k) = \text{sign}(\mathcal{X}(i, j, k))(\max\{|\mathcal{X}(i, j, k)| - v, 0\}). \quad (12)$$

\mathcal{S} Sub-problem: The \mathcal{S} sub-problem is

$$\min_{\mathcal{S}} \|\mathcal{Y} - f_{\Theta^t}(\mathcal{Z}) - \mathcal{S}\|_F^2 + \alpha_3 \|\mathcal{S}\|_{\ell_1}, \quad (13)$$

Algorithm 1 HSI Mixed Noise Removal Using S2DIP

Input: Noisy HSI \mathcal{Y} , $t_{max} = 7000$, $r = 0.001$;

Initialization: Randomly initialize Θ , $\Lambda_i = \mathbf{0}$, $t = 0$, $r' = r$;

- 1: **while** $t \leq t_{max}$ and $r' \geq r$ **do**
- 2: Update \mathcal{V}_i ($i = 1, 2, 3, 4$) via (11);
- 3: Update \mathcal{S} via (14);
- 4: Update Θ via (15);
- 5: Update Λ_i ($i = 1, 2, 3, 4$) via (16);
- 6: $r' = \frac{\|f_{\Theta^{t+1}}(\mathcal{Z}) - f_{\Theta^t}(\mathcal{Z})\|_F^2}{\|f_{\Theta^t}(\mathcal{Z})\|_F^2}$;
- 7: $t = t + 1$;
- 8: **end while**

Output: The denoising HSI $\mathcal{X} = f_{\Theta}(\mathcal{Z})$;

which can be exactly solved by

$$\mathcal{S}^{t+1} = \text{Soft}_{2\alpha_3}(\mathcal{Y} - f_{\Theta^t}(\mathcal{Z})). \quad (14)$$

 Θ **Sub-problem** The Θ sub-problem is

$$\begin{aligned} \min_{\Theta} & \|\mathcal{Y} - f_{\Theta}(\mathcal{Z}) - \mathcal{S}^t\|_F^2 + \frac{\mu}{2} (\|\nabla_x(f_{\Theta}(\mathcal{Z})) - \mathcal{D}_1^t\|_F^2 \\ & + \|\nabla_y(f_{\Theta}(\mathcal{Z})) - \mathcal{D}_2^t\|_F^2 + \|\nabla_x \nabla_z(f_{\Theta}(\mathcal{Z})) - \mathcal{D}_3^t\|_F^2 \\ & + \|\nabla_y \nabla_z(f_{\Theta}(\mathcal{Z})) - \mathcal{D}_4^t\|_F^2), \end{aligned} \quad (15)$$

 where $\mathcal{D}_i^t = \mathcal{V}_i^t - \frac{\Lambda_i^t}{\mu}$. We adopt the adaptive moment estimation (Adam) [50] to update Θ . Specifically, we employ one gradient descent step by using the Adam in each update. The loss functions are all F -norm-based functions, so the gradient can be easily computed in current deep learning frameworks.

 Λ **Updating** The Lagrange multipliers are updated as

$$\begin{cases} \Lambda_1^{t+1} = \Lambda_1^t + \mu(\nabla_x(f_{\Theta^t}(\mathcal{Z})) - \mathcal{V}_1^t) \\ \Lambda_2^{t+1} = \Lambda_2^t + \mu(\nabla_y(f_{\Theta^t}(\mathcal{Z})) - \mathcal{V}_2^t) \\ \Lambda_3^{t+1} = \Lambda_3^t + \mu(\nabla_x \nabla_z(f_{\Theta^t}(\mathcal{Z})) - \mathcal{V}_3^t) \\ \Lambda_4^{t+1} = \Lambda_4^t + \mu(\nabla_y \nabla_z(f_{\Theta^t}(\mathcal{Z})) - \mathcal{V}_4^t). \end{cases} \quad (16)$$

The ADMM algorithm is summarized in Algorithm 1.

E. The Automatic Stopping Criterion

We introduce an automatic stopping criterion to demonstrate that the proposed S2DIP can be automatically terminated based on its convergence property. Specifically, we use the relative error

$$\mathbf{RelErr} = \frac{\|f_{\Theta^{t+1}}(\mathcal{Z}) - f_{\Theta^t}(\mathcal{Z})\|_F^2}{\|f_{\Theta^t}(\mathcal{Z})\|_F^2} \quad (17)$$

 and iteration step to evaluate the convergence degree. Here, $f_{\Theta^t}(\mathcal{Z}) \in \mathbb{R}^{H \times W \times B}$ denotes the t -th network output. We set two parameters r and t_{max} as the tolerance of **RelErr** and the maximum number of iteration steps, respectively. The iteration will be terminated if: 1) **RelErr** of the t -th iteration is lower than r , or 2) the iteration number t exceeds t_{max} . Cooperatively, **RelErr** evaluates the convergent degree of the optimization process while t_{max} guarantees the final stopping of the iteration.

We use S2DIP* to denote the highest peak signal-to-noise ratio (PSNR) value of the proposed method and use S2DIP to denote the proposed method using the automatic stopping

TABLE I

 THE SIMULATED NOISY SETTING. σ DENOTES THE STANDARD DEVIATION. p DENOTES THE SAMPLING RATE. s_1 AND s_2 DENOTE THE NUMBERS OF STRIPES AND DEADLINES IN EACH CORRUPTED BAND, RESPECTIVELY.

Case	Gaussian noise		Impulse noise		Stripe		Deadline	
	added band	σ	added band	p	added band	s_1	added band	s_2
Case 1	all bands	0.2	--	--	--	--	--	--
Case 2	all bands	0.1	all bands	0.1	--	--	--	--
Case 3	all bands	0.1	all bands	0.1	40%	[6, 15]	--	--
Case 4	all bands	0.1	all bands	0.1	--	--	50%	[6, 10]
Case 5	all bands	0.1	all bands	0.1	40%	[6, 15]	50%	[6, 10]

criterion. If the performance of S2DIP is comparable to that of S2DIP*, it means that S2DIP converges to the point with the highest PSNR value, which alleviates the semi-convergence of DIP. It is worth emphasizing that the original DIP could not use such stopping criterion since DIP suffers from semi-convergence. Using such stopping criterion for DIP would result in poor performance, as DIP always converges to a noisy HSI. For convenience, we report the highest PSNR value of DIP in the experiments.

IV. EXPERIMENTS

Both simulation experiments and real data experiments are involved to verify the validity of the proposed method. The competing methods include the matrix low-rankness-based method LRMR [18], the tensor low-rankness and total variation-based method LRTDTV [20], the supervised deep CNN-based method HSID-CNN [39], and the unsupervised DIP methods that based on 2D convolution and 3D convolution (termed as DIP 2D and DIP 3D) [1], [42]. The hyperparameters of model-based methods are tuned based on their best PSNR values. The results of HSID-CNN are obtained by using the pre-trained model provided by the author.

 For simulation experiments, we adopt sub-images of HSIs *WDC mall*, *Pavia*, *Indian pines*, and *Salinas*¹ with size $256 \times 256 \times 32$, $192 \times 192 \times 32$, $128 \times 128 \times 32$, and $192 \times 192 \times 32$, respectively, to generate simulated noisy HSIs. Additionally, multispectral images (MSIs) including *Trash*, *Board*², *Balloons*, and *Cups*³ [51] are adopted to verify the generalization ability of our method. The size of *Trash* and *Board* is $256 \times 256 \times 32$ and the size of the *Balloons* and *Cups* is $256 \times 256 \times 31$. For all selected images, five noisy cases are established, see Table I. Based on the noisy setting in Table I, all noise is randomly performed on the ground-truth (GT) images. For cases with deadlines, we change the fidelity term of our method to $\|\mathcal{M} \odot (\mathcal{Y} - \mathcal{X}) - \mathcal{S}\|_F^2$, where \mathcal{M} denotes the mask whose entries on the positions of deadlines are set to 0 and other entries are set to 1, i.e., the removal of deadlines can be seen as an inpainting problem. The inpainting problem can be well addressed by the deep prior of the CNN [1], [42]. Here, \odot denotes the element-wise product. We empirically set the tolerance of **RelErr** (i.e., r) as 0.01, and t_{max} as 7000,

¹<http://www.ehu.es/ccwintco/index.php?title=HyperspectralRemoteSensingScenes>
²<https://sites.google.com/site/hyperspectralcolorimaging/dataset/general-scenes>
³<https://www.cs.columbia.edu/CAVE/databases/multispectral/>

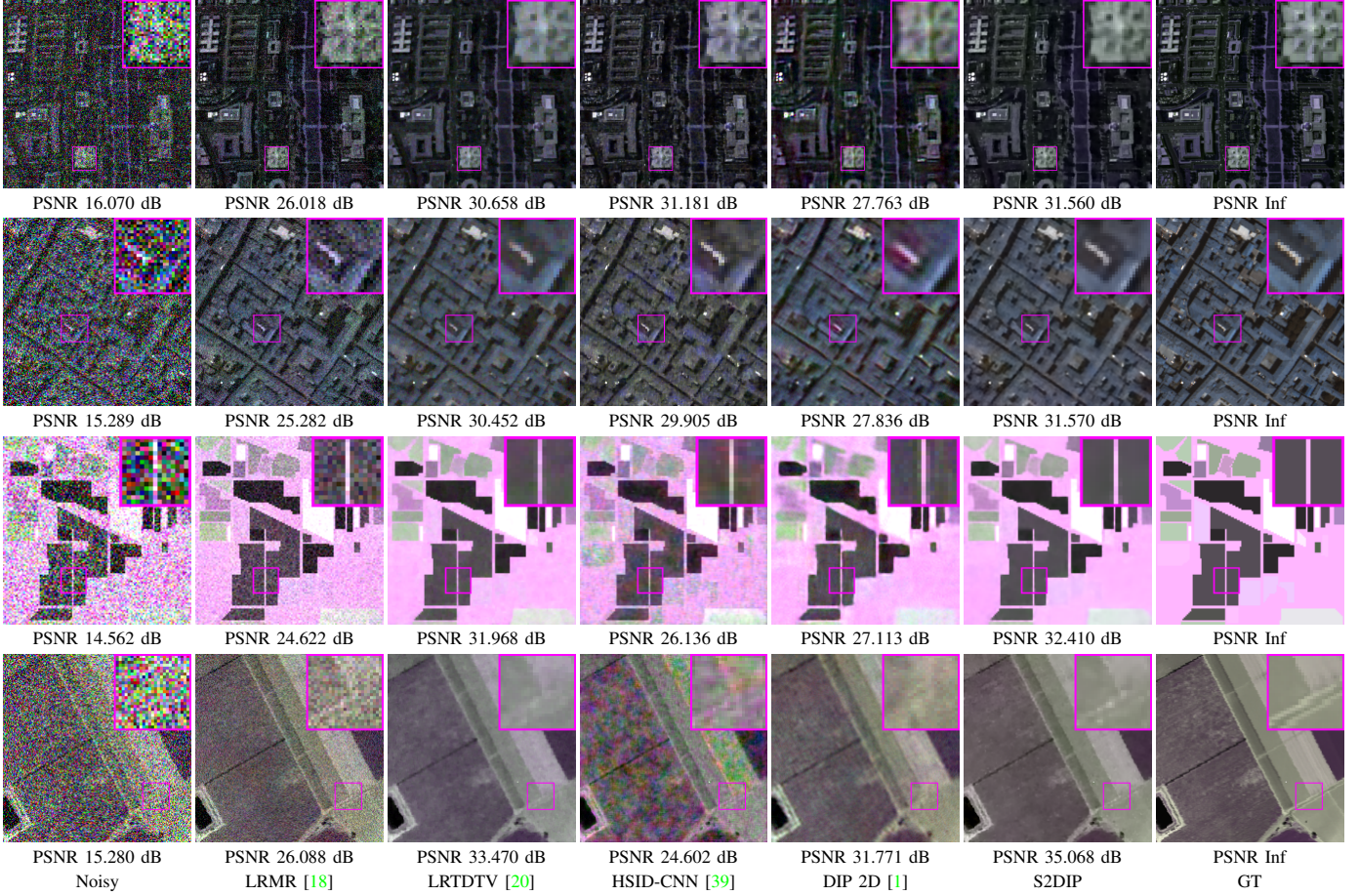


Fig. 3. The denoising HSIs by different methods for **Case 1**. Each row from top to down lists *WDC mall* consisted of the 5-th, 15-th, and 30-th bands, *Pavia* consisted of the 5-th, 15-th, and 30-th bands, *Indian pines* consisted of the 15-th, 25-th, and 29-th bands, and *Salinas* consisted of the 18-th, 25-th, and 32-th bands.

TABLE II

THE QUANTITATIVE RESULTS BY DIFFERENT METHODS ON HSIS. THE **BEST** VALUE IS HIGHLIGHTED BY **BOLDFACE**. THE SECOND-BEST VALUE IS HIGHLIGHTED BY UNDERLINE.

Case		Case 1			Case 2			Case 3			Case 4			Case 5		
Data	Method	PSNR	SSIM	SAM	PSNR	SSIM	SAM	PSNR	SSIM	SAM	PSNR	SSIM	SAM	PSNR	SSIM	SAM
<i>WDC mall</i>	LRMR	26.018	0.767	0.563	29.869	0.887	0.335	27.090	0.835	0.461	29.321	0.880	0.358	26.658	0.828	0.487
	LRTDTV	30.658	0.899	0.218	31.625	0.917	0.236	31.433	0.905	0.271	30.965	0.904	0.272	30.615	0.889	0.311
	HSID-CNN	31.181	0.918	0.210	25.222	0.792	0.234	23.237	0.740	0.306	25.424	0.791	0.244	23.391	0.737	0.313
	DIP 2D	27.763	0.826	0.265	24.621	0.727	0.172	22.753	0.642	0.240	24.591	0.737	0.202	22.607	0.617	0.221
	DIP 3D	27.784	0.828	0.264	24.714	0.744	0.210	23.306	0.689	0.244	24.553	0.731	0.199	23.116	0.675	0.225
	S2DIP	31.560	0.920	0.112	32.503	0.931	0.102	32.333	0.930	0.112	32.585	0.932	0.102	32.004	0.924	0.111
	S2DIP*	31.740	0.922	0.113	32.886	0.937	0.105	32.620	0.933	0.110	32.662	0.933	0.104	32.442	0.931	0.116
<i>Pavia</i>	LRMR	25.282	0.751	0.259	29.467	0.886	0.153	27.040	0.836	0.240	28.050	0.863	0.193	25.843	0.811	0.269
	LRTDTV	30.452	0.901	0.103	31.634	0.924	0.105	31.243	0.907	0.131	30.105	0.900	0.148	29.417	0.878	0.175
	HSID-CNN	29.905	0.906	0.114	26.430	0.856	0.124	24.307	0.815	0.168	26.513	0.842	0.146	24.611	0.797	0.191
	DIP 2D	27.836	0.845	0.118	25.472	0.808	0.112	23.797	0.740	0.124	25.480	0.811	0.098	23.738	0.740	0.128
	DIP 3D	27.781	0.840	0.141	25.844	0.822	0.111	24.239	0.782	0.109	25.571	0.810	0.106	24.277	0.784	0.122
	S2DIP	31.570	0.928	0.062	32.790	0.943	0.058	32.554	0.945	0.063	32.839	0.943	0.060	32.366	0.940	0.065
	S2DIP*	31.674	0.930	0.061	33.016	0.946	0.058	32.710	0.945	0.061	32.981	0.945	0.058	32.437	0.941	0.064
<i>Indian pines</i>	LRMR	24.622	0.725	0.135	28.731	0.859	0.084	27.712	0.844	0.108	23.256	0.756	0.203	23.108	0.757	0.201
	LRTDTV	31.968	0.952	0.050	33.881	0.965	0.043	32.953	0.952	0.061	28.071	0.894	0.129	27.982	0.886	0.146
	HSID-CNN	26.136	0.846	0.113	25.080	0.844	0.111	24.217	0.833	0.124	21.286	0.750	0.181	21.239	0.745	0.190
	DIP 2D	27.113	0.882	0.088	26.193	0.874	0.078	24.700	0.832	0.122	25.886	0.867	0.077	24.434	0.831	0.112
	DIP 3D	26.972	0.864	0.092	26.333	0.863	0.076	25.356	0.847	0.089	26.159	0.869	0.069	25.150	0.850	0.090
	S2DIP	32.410	0.967	0.040	35.120	0.984	0.035	34.009	0.983	0.040	34.584	0.983	0.037	33.522	0.978	0.043
	S2DIP*	32.710	0.968	0.037	35.364	0.984	0.034	34.860	0.984	0.038	35.181	0.984	0.037	33.769	0.978	0.042
<i>Salinas</i>	LRMR	26.088	0.652	0.148	29.786	0.808	0.098	27.287	0.757	0.172	28.354	0.782	0.166	25.422	0.717	0.228
	LRTDTV	33.470	0.904	0.074	34.360	0.905	0.075	33.471	0.887	0.091	32.013	0.871	0.133	31.915	0.847	0.165
	HSID-CNN	24.602	0.713	0.244	23.273	0.673	0.266	22.040	0.632	0.291	22.824	0.653	0.287	21.270	0.596	0.317
	DIP 2D	31.771	0.891	0.069	27.592	0.812	0.116	25.885	0.787	0.152	27.527	0.812	0.114	25.492	0.782	0.152
	DIP 3D	32.729	0.916	0.058	28.141	0.840	0.109	25.983	0.807	0.134	28.211	0.846	0.104	26.185	0.806	0.141
	S2DIP	35.068	0.945	0.039	35.997	0.954	0.036	35.123	0.950	0.042	36.056	0.956	0.034	35.084	0.948	0.043
	S2DIP*	35.224	0.946	0.041	36.223	0.956	0.037	35.474	0.952	0.041	36.212	0.957	0.036	35.259	0.951	0.043

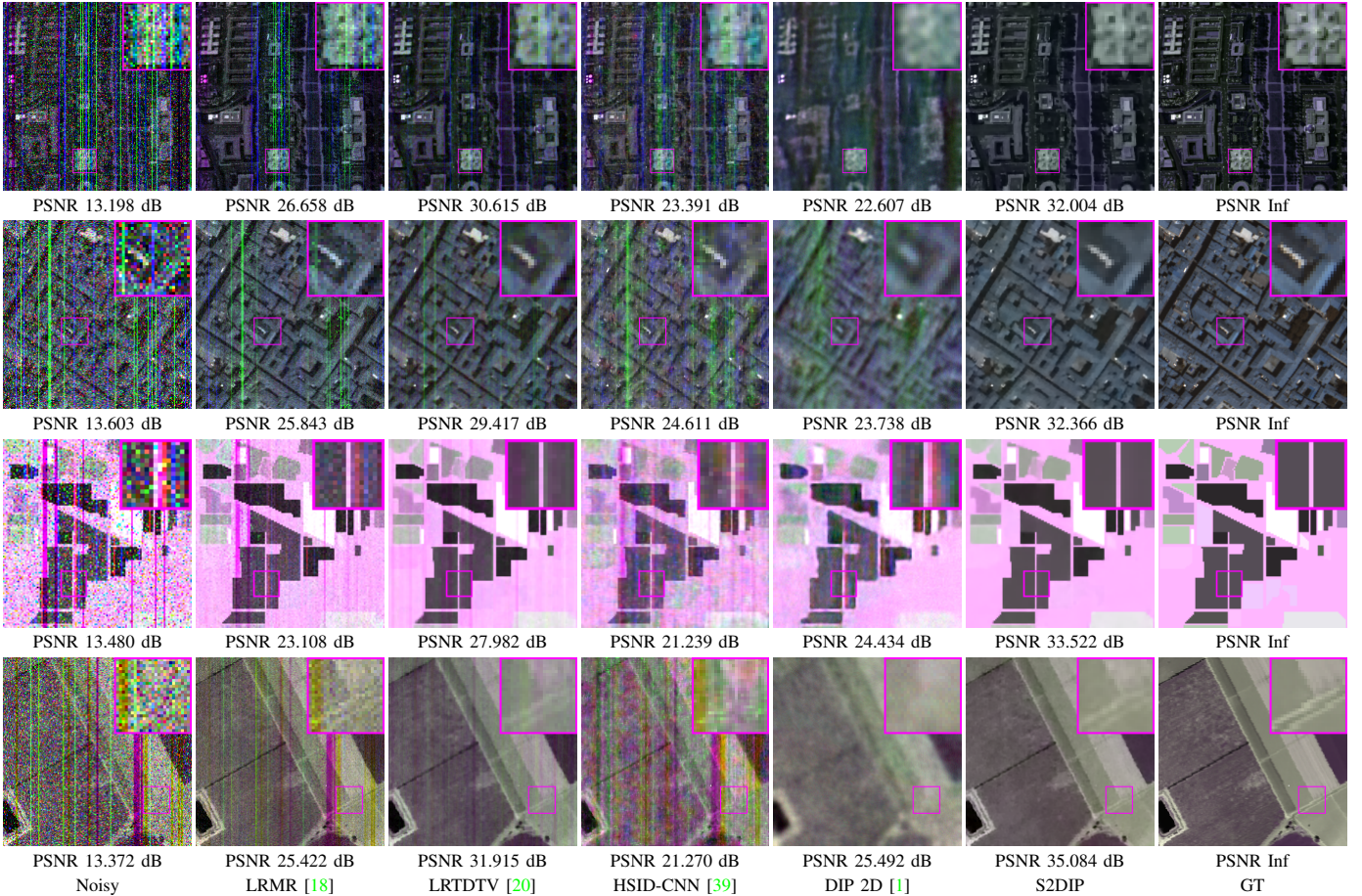


Fig. 4. The denoising HSIs by different methods for **Case 5**. Each row from top to down lists *WDC mall* consisted of the 5-th, 15-th, and 30-th bands, *Pavia* consisted of the 5-th, 15-th, and 30-th bands, *Indian pines* consisted of the 15-th, 25-th, and 29-th bands, and *Salinas* consisted of the 18-th, 25-th, and 32-th bands.

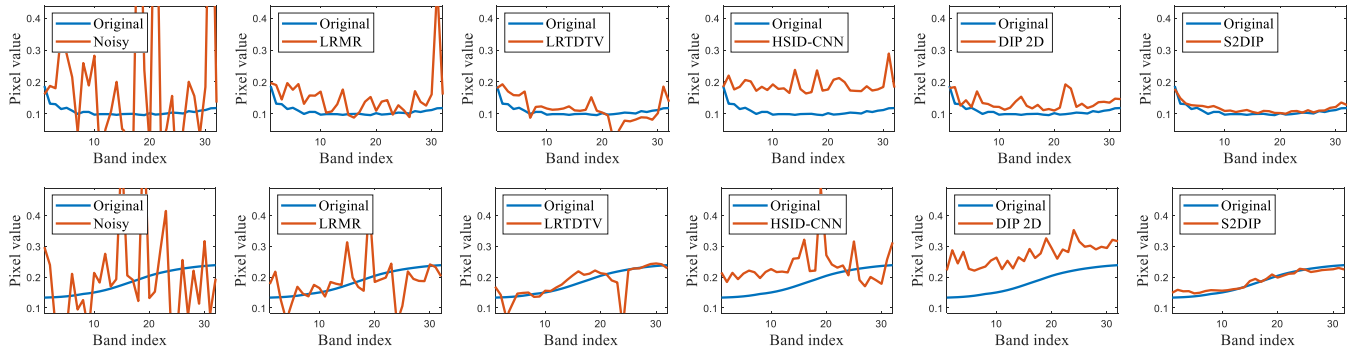


Fig. 5. The spectral curves of the recovered results by different methods on HSIs *WDC mall* and *Pavia* for **Case 5**.

which provides good termination points. In addition, we set our hyperparameters $\alpha_1 = 0.1$, $\alpha_2 = 0.1$, and $\alpha_3 = 0.01$ for **Case 2-5**. For **Case 1**, we change $\alpha_3 = 10$ and other parameters remain the same.

In simulation experiments, the denoising results are numerically evaluated by PSNR, structure similarity (SSIM), and spectral angle mapper (SAM) [52]. It is worth noting that higher PSNR and SSIM values represent better performance while lower SAM values represent better performance.

In real experiments, noisy HSIs *Urban* of size $288 \times 288 \times 210$ with its band 134 to band 165 and *Indian*⁴ of size

$128 \times 128 \times 220$ with its band 1 to band 32 are included. The hyperparameters of our method for real experiments are $\alpha_1 = 0.1$, $\alpha_2 = 0.1$, and $\alpha_3 = 0.01$.

All the experiments are conducted on the platform of Windows 10 with Intel Core i5-9400f CPU, Nvidia RTX 2080 GPU, and 16 GB RAM.

A. Simulation Experiments

The numerical results on HSIs are illustrated in Table II. We can discover that S2DIP* outperforms competing methods in terms of PSNR. S2DIP is also competitive with PSNR a little lower than S2DIP*, which shows that S2DIP has convergence

⁴<https://pur.purdue.edu/publications/1947/1>

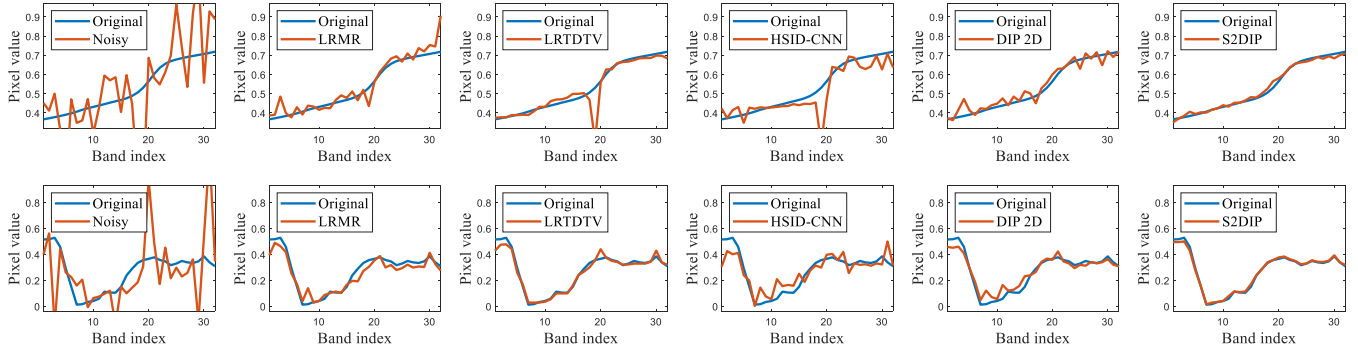


Fig. 6. The spectral curves of the recovered results by different methods on HSIs *Indian pines* and *Salinas* for **Case 5**.

TABLE III
THE QUANTITATIVE RESULTS BY DIFFERENT METHODS ON MSIS. THE **BEST** VALUE IS HIGHLIGHTED BY **BOLDFACE**. THE SECOND-BEST VALUE IS HIGHLIGHTED BY UNDERLINED.

Case		Case 1			Case 2			Case 3			Case 4			Case 5		
Data	Method	PSNR	SSIM	SAM	PSNR	SSIM	SAM	PSNR	SSIM	SAM	PSNR	SSIM	SAM	PSNR	SSIM	SAM
Trash	LRMR	25.437	0.642	0.302	29.548	0.820	0.170	27.210	0.780	0.261	27.898	0.804	0.202	25.714	0.753	0.304
	LRTDTV	29.812	0.922	0.145	32.088	0.932	0.130	31.300	0.916	0.154	30.939	<u>0.915</u>	0.157	30.377	0.903	0.176
	HSID-CNN	28.389	0.857	0.168	25.111	0.785	0.183	23.727	0.749	0.219	24.857	0.776	0.196	23.325	0.726	0.235
	DIP 2D	31.291	0.922	<u>0.105</u>	26.985	0.865	0.131	25.530	0.850	0.145	27.145	0.877	<u>0.109</u>	25.211	0.846	0.142
	DIP 3D	29.895	0.931	0.134	26.909	0.901	0.129	24.979	0.873	0.141	26.806	0.891	0.137	24.820	0.861	0.155
	S2DIP	<u>33.352</u>	<u>0.971</u>	0.078	<u>35.549</u>	<u>0.978</u>	<u>0.064</u>	<u>34.891</u>	<u>0.976</u>	0.068	<u>35.488</u>	0.978	0.064	<u>34.694</u>	<u>0.975</u>	<u>0.073</u>
	S2DIP*	33.537	0.972	0.078	35.716	0.978	0.062	35.112	0.977	<u>0.069</u>	35.690	0.978	0.064	34.985	0.976	0.071
Borad	LRMR	25.610	0.687	0.333	29.552	0.841	0.191	27.256	0.803	0.274	27.596	0.820	0.227	25.622	0.778	0.330
	LRTDTV	28.938	<u>0.904</u>	0.137	31.032	0.917	0.150	30.645	<u>0.908</u>	0.166	30.150	0.901	0.179	29.630	0.884	0.218
	HSID-CNN	28.019	0.856	0.178	24.984	0.785	0.188	23.312	0.743	0.220	24.444	0.769	0.208	23.031	0.729	0.247
	DIP 2D	30.258	0.888	0.136	26.765	0.842	0.134	25.226	0.814	0.138	26.886	0.840	<u>0.137</u>	25.167	0.811	0.160
	DIP 3D	29.768	0.899	0.145	26.886	0.859	0.149	25.297	0.834	0.156	26.562	0.860	<u>0.137</u>	25.225	0.833	0.164
	S2DIP	<u>31.811</u>	0.939	0.102	<u>33.600</u>	<u>0.956</u>	0.085	<u>33.272</u>	0.955	<u>0.091</u>	<u>33.390</u>	<u>0.956</u>	0.085	<u>33.188</u>	<u>0.953</u>	0.090
	S2DIP*	31.925	0.939	<u>0.103</u>	33.712	0.957	<u>0.086</u>	33.383	0.955	0.090	33.634	0.957	0.085	33.289	0.955	<u>0.091</u>
Balloons	LRMR	28.311	0.794	0.223	27.891	0.734	0.291	27.618	0.758	0.299	26.801	0.729	0.315	28.938	0.801	0.254
	LRTDTV	33.928	0.949	0.235	35.406	0.948	0.193	34.788	<u>0.937</u>	0.203	34.359	0.944	0.210	34.154	0.933	0.226
	HSID-CNN	28.452	0.839	0.317	24.586	0.680	0.338	22.761	0.625	0.366	24.130	0.669	0.353	22.659	0.624	0.408
	DIP 2D	33.989	0.948	0.189	27.114	0.822	0.224	25.204	0.786	0.262	27.182	0.818	0.239	25.450	0.791	0.283
	DIP 3D	33.343	0.940	0.217	27.257	0.817	0.242	25.110	0.773	0.254	27.033	0.824	0.241	25.319	0.786	0.275
	S2DIP	<u>36.610</u>	<u>0.978</u>	<u>0.117</u>	<u>38.482</u>	<u>0.980</u>	<u>0.101</u>	<u>37.888</u>	0.976	0.113	<u>38.216</u>	<u>0.978</u>	<u>0.104</u>	<u>37.367</u>	<u>0.971</u>	<u>0.125</u>
	S2DIP*	37.435	0.980	0.115	39.152	0.985	0.094	38.082	0.976	<u>0.114</u>	38.828	0.983	0.100	37.881	0.973	0.121
Cups	LRMR	27.042	0.752	0.071	28.417	0.770	0.111	29.147	0.812	0.093	26.023	0.734	0.159	28.783	0.834	0.092
	LRTDTV	33.804	<u>0.963</u>	0.079	35.908	<u>0.961</u>	0.064	35.601	<u>0.959</u>	0.066	34.547	<u>0.950</u>	0.076	33.867	<u>0.942</u>	0.082
	HSID-CNN	28.739	0.854	0.109	26.626	0.827	0.124	25.617	0.809	0.140	25.418	0.795	0.155	24.483	0.770	0.175
	DIP 2D	32.473	0.942	0.076	29.810	0.930	0.075	27.709	0.916	0.098	28.963	0.926	0.072	27.801	0.912	0.106
	DIP 3D	32.254	0.940	0.074	29.403	0.929	0.075	28.183	0.910	0.093	29.440	0.927	0.077	27.844	0.920	<u>0.081</u>
	S2DIP	<u>36.376</u>	0.983	0.036	<u>38.560</u>	0.989	0.030	<u>37.882</u>	0.988	<u>0.035</u>	<u>38.169</u>	0.989	0.031	<u>37.834</u>	0.988	0.034
	S2DIP*	36.469	0.983	<u>0.037</u>	38.766	0.989	<u>0.031</u>	38.160	0.988	0.033	38.605	0.989	<u>0.032</u>	38.147	0.988	0.034

property to stably handle the mixed noise removal under unsupervised conditions, which avoids the semi-convergence of DIP.

It is notable that the SAM values of the proposed method are also superior to competing methods. This mainly attributes to the spatial-spectral constraint of the proposed framework, where high-quality spatial-spectral correlation and spectral fidelity are ensured.

In Fig. 3, the denoising results on HSIs for **Case 1** are displayed. Since **Case 1** only contains Gaussian noise, LRTDTV, HSID-CNN, and S2DIP can both remove the noise well and obtain good visual quality, while S2DIP achieves better PSNR values. We subsequently illustrate the denoising results on HSIs for **Case 5** in Fig. 4, as **Case 5** contains the most complex noise. We can see that LRM, which delivers the low-rankness by matrix, is hard to totally remove the mixed noise. LRTDTV considers the tensor low-rankness, thus it achieves noise removal in partial bands, but also fails to totally

remove the stripes and impulses. The supervised HSID-CNN is trained on data with only Gaussian noise. Thus, it is hard to deal with strong complex simulated noise. DIP 2D and DIP 3D are hard to fit the signal part of the observation before fitting the complex noise. Thus, DIP could not well recover clean HSIs. The proposed S2DIP achieves the best performance compared with competing methods, where the mixed noise is considerably removed and the image details are well preserved. The good visual quality of the denoising results of S2DIP can attribute to the combination of the expressive power of the CNN and the hand-crafted priors, which ensures the recovery quality.

Next, we display the spectral curves of the recovered results by different methods on HSIs in Fig. 5 and Fig. 6. The less oscillating spectral curves of the denoising results by S2DIP verify that the spectral fidelity is well-preserved, which outperforms competing methods. The integration of deep prior brought by the CNN and the spatial-spectral constraint by the

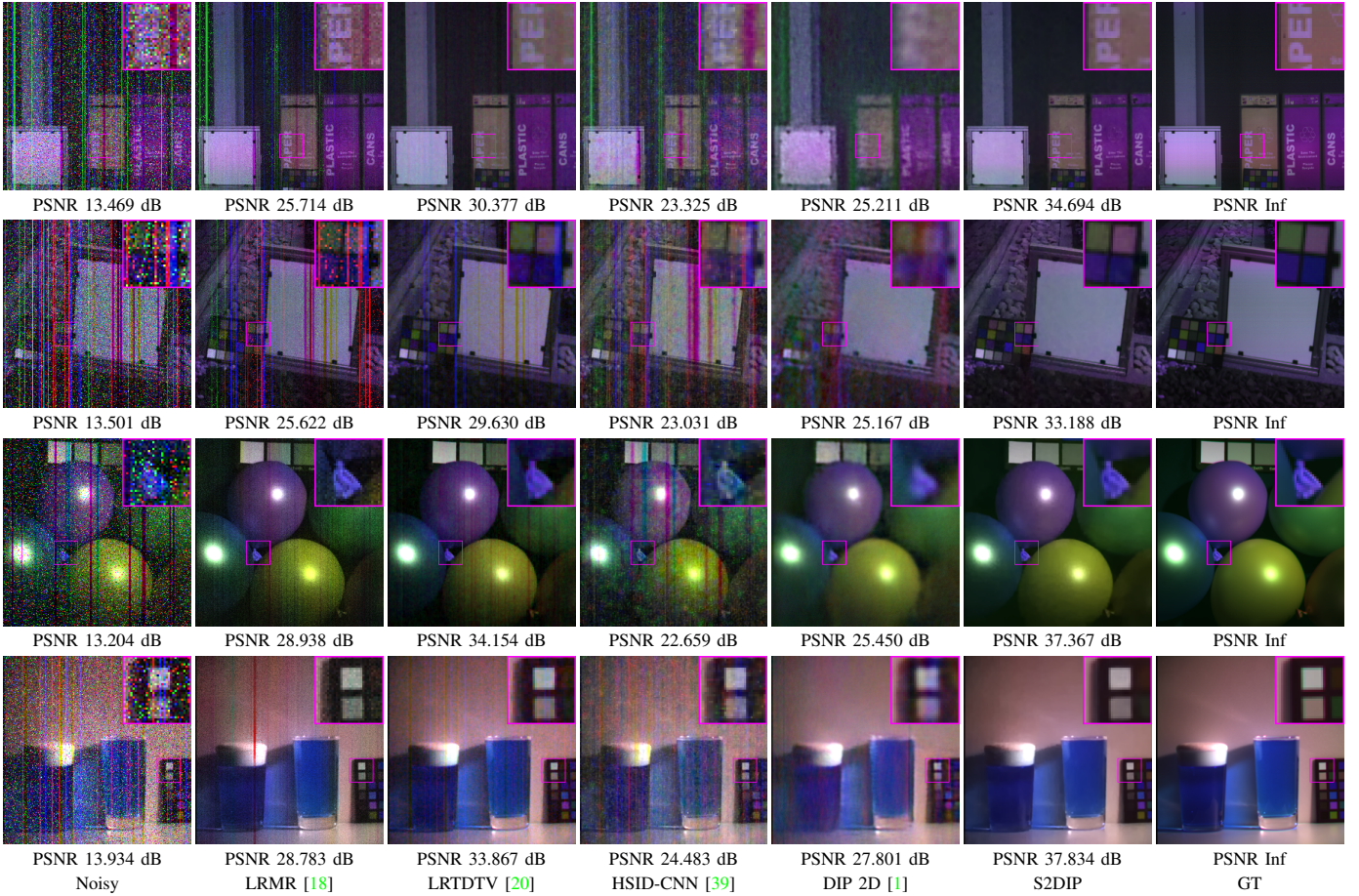


Fig. 7. The denoising MSIs by different methods for **Case 5**. Each row from top to down lists *Trash* consisted of the 5-th, 15-th, and 25-th bands, *Borad* consisted of the 5-th, 15-th, and 25-th bands, *Balloons* consisted of the 1-st, 10-th, and 30-th bands, and *Cups* consisted of the 1-st, 10-th, and 30-th bands.

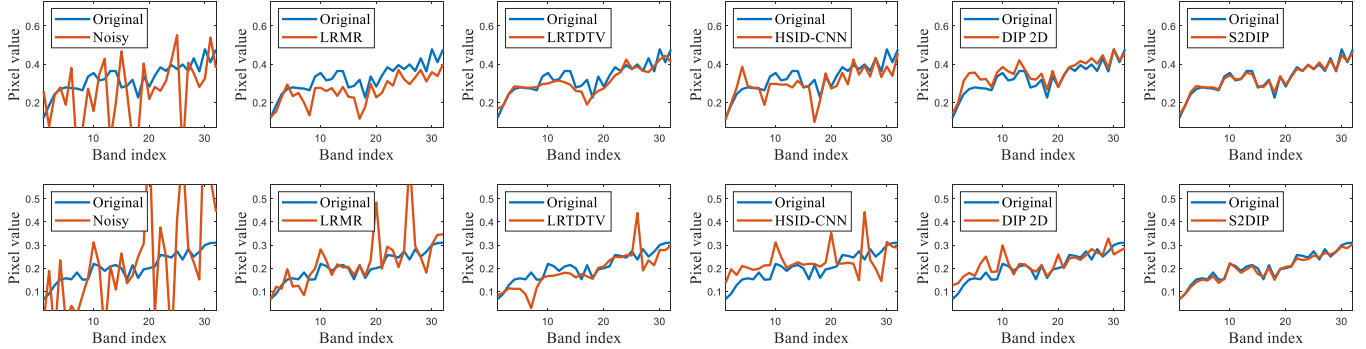


Fig. 8. The spectral curves of the recovered results by different methods on MSIs *Trash* and *Borad* for **Case 5**.

SSTV regularization contributes to this phenomenon.

Then, we illustrate the denoising quantitative results by different methods on MSIs in Table III. We can see that S2DIP and S2DIP* considerably outperforms competing methods, which verify the generalization ability and effectiveness of the proposed method for various data.

The denoising results by different methods on MSIs for **Case 5** are displayed in Fig. 7. We can observe that S2DIP recovers the MSI and removes the complex noise well. LRM and LRTDTV could not totally remove the noise. The HSID-CNN is trained on Gaussian noisy HSIs and thus it is hard to deal with such mixed noise in MSIs. As compared, S2DIP has a better generalization ability for mixed noise in various types

of data. DIP methods remove the noise but miss some image details and edges. Note that the results of DIP are selected by referring to the GT images on the highest PSNR values. In contrast, the results of S2DIP are automatically selected based on the stopping criterion. This verifies that the proposed S2DIP favorably addresses the semi-convergence of DIP and largely enhances the denoising ability of DIP.

Finally, we plot the spectral curves of the recovered MSIs by different methods in Fig. 8 and Fig. 9. We can see that S2DIP better preserves the nonlinear spectral curves. This could attribute to the integration of hand-crafted priors and the DIP, where the nonlinear modeling ability of CNN and the spatial-spectral constraint are well combined.

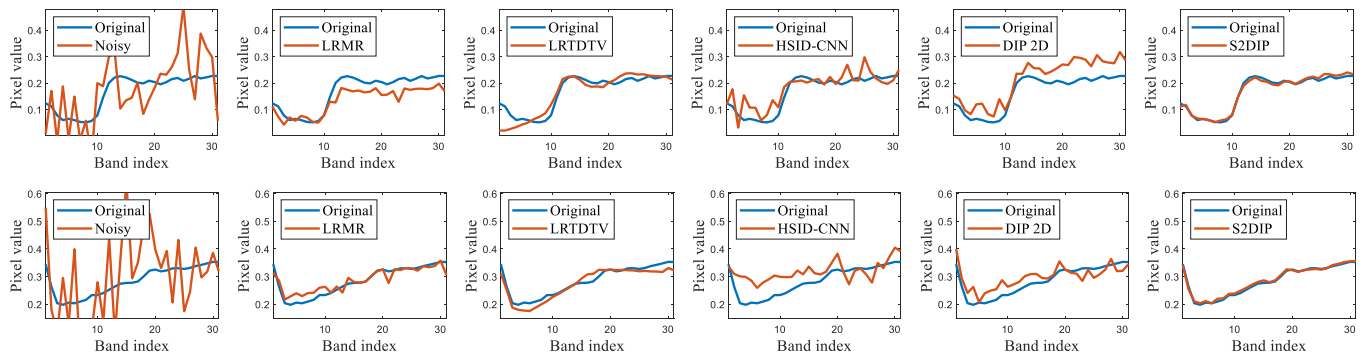


Fig. 9. The spectral curves of the recovered results by different methods on MSIs *Balloons* and *Cups* for **Case 5**.

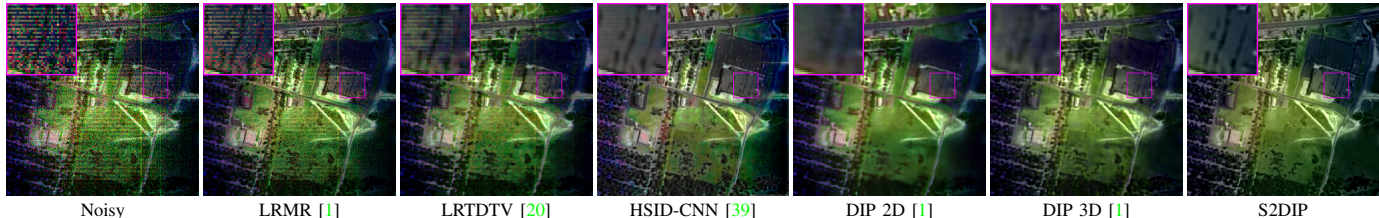


Fig. 10. The recovered results by different methods for real-world noisy HSI *Urban* (The pseudo images consisted of the 139-th, 150-th, and 151-th bands).

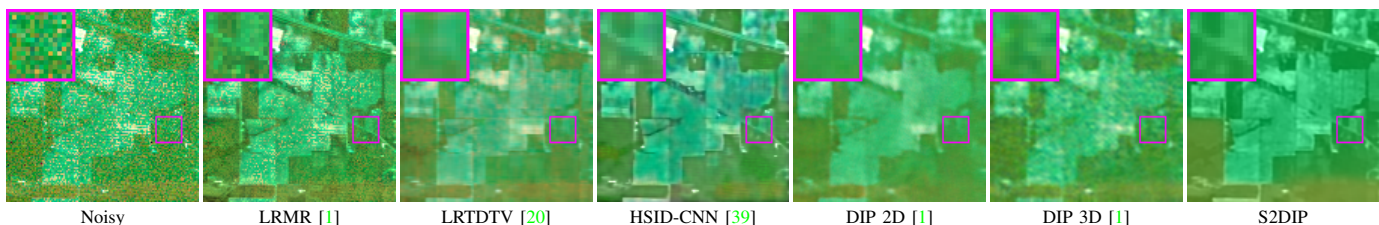


Fig. 11. The recovered results by different methods for real-world noisy HSI *Indian* (The pseudo images consisted of the 1-st, 2-nd, and 3-rd bands).

B. Real Experiments

The denoising results for real-world noisy HSI *Urban* are displayed in Fig. 10. We can see that S2DIP shows better performance for removing the complex noise. Specifically, S2DIP removes the noise and preserves the image details well. LRMR and LRTDTV could not totally remove the mixed noise. DIP has over-smooth results. HSID-CNN achieves considerable results. But if one looks closely, the result of HSID-CNN remain some stripe noise.

The denoising results for *Indian* are illustrated in Fig. 11. We can see that LRTDTV and DIP 2D both remove the strong noise but miss some image details. HSID-CNN removes the complex noise and achieves good results. S2DIP also successfully and reasonably restores the image structure, where the complex noise is removed and the image details and colors are well preserved.

The good performance of S2DIP for real noise removal is mainly due to the combination of deep prior and hand-crafted priors. The natural image structure can be well preserved by the DIP and the mixed noise can be fully removed by the spatial-spectral constraint and the robust noise modeling.

We can find that in real experiments, the performance of HSID-CNN is much better than that of simulation experiments. This is because that the number of noisy bands in real noisy HSIs is relatively small. HSID-CNN can explore the spatial-spectral information from other clean bands for denoising. The

proposed unsupervised S2DIP could achieve even better results than the supervised HSID-CNN for real noise removal. Also, the denoising results by S2DIP can be selected by setting different model parameters. Supervised methods like HSID-CNN use one well-trained CNN for denoising and thus could only have one chance for denoising. In other words, S2DIP may be relatively more flexible in real applications.

V. DISCUSSIONS

A. Effectiveness of Deep Prior

Our method simultaneously uses the unsupervised deep prior, the spatial-spectral image prior, and the sparse noise prior. In this section, we illustrate the effectiveness of the deep prior. Specifically, we remove the deep prior of CNN in the proposed model (7) to clarify its influence. Here, the underlying clean HSI could be updated via ADMM. Note that the proposed method degenerates to the hybrid spatial-spectral total variation (HSSTV) [13] method without the deep prior. The HSSTV considers the TV and SSTV on the clean HSI and remove the sparse noise via minimizing its ℓ_1 -norm. The difference between HSSTV and the proposed method is that we additionally use the DIP while HSSTV just employs TV and SSTV regularizers in a traditional optimization model.

We conduct the comparison between HSSTV and S2DIP on *Balloons* and *Cups* for **Case 5**. Fig. 12 shows the denoising results. We can see that S2DIP removes the complex noise

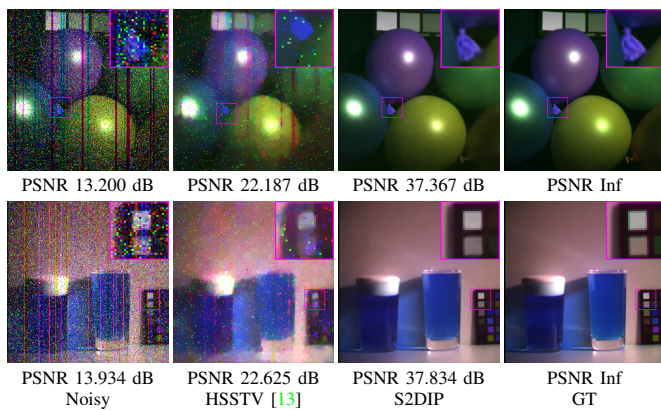


Fig. 12. The denoising MSIs *balloons* and *Cups* consisted of the 1-st, 10-th, and 30-th bands by different methods.

TABLE IV

THE QUANTITATIVE RESULTS BY DIFFERENT METHODS. S2DIP WO. SPARSITY DENOTES THE PROPOSED METHOD WITHOUT THE SPARSE TERM. S2DIP WO. SSTV DENOTES THE PROPOSED METHOD WITHOUT THE TV AND SSTV TERM.

Method	<i>Balloons Case 5</i>			<i>Cups Case 5</i>		
	PSNR	SSIM	SAM	PSNR	SSIM	SAM
S2DIP wo. sparsity	26.116	0.816	0.258	28.952	0.955	0.076
S2DIP wo. SSTV	34.775	0.949	0.167	33.729	0.958	0.059
S2DIP	37.367	0.971	0.125	37.834	0.988	0.034

and preserves the image details and edges well. In contrast, HSSTV could not completely remove the impulse noise and stripes, while the image details are also missed. This verifies the effectiveness of the deep prior, which can capture the natural image structure. S2DIP faithfully combines the deep prior of CNN and the hand-crafted prior, taking both advantages of the high representation ability of CNN and the spatial-spectral constraint delivered by the SSTV in an unsupervised manner.

B. Effectiveness of Hand-Crafted Priors

To address the semi-convergence of DIP and improve its denoising performance on HSI, we suggest two hand-crafted priors in DIP, i.e., the SSTV term and the sparse term. This section verifies their effectiveness. Specifically, we compare the proposed method with and without the SSTV term and the sparse term to clarify their influence. The results are illustrated in Table IV. We can see that S2DIP considerably outperforms S2DIP wo. SSSTV and S2DIP wo. sparsity, which verifies the effectiveness of the hand-crafted priors in the DIP framework. The deep prior, the spatial-spectral local smooth prior, and the sparse noise prior are organically combined to handle the mixed noise removal in HSI. Notably, S2DIP wo. sparsity has relatively weak performance, which shows that the sparse modeling of the complex noise is very essential. In fact, the HSI noise in **Case 5** contains many sparse outliers, which can not be fully removed if only considering Gaussian noise. Thus, introducing the sparse term can largely improve the robustness and effectiveness of the unsupervised DIP for HSI mixed noise removal.

C. Influence on Subsequent Applications

This section verifies that using S2DIP for HSI denoising can improve the performance of subsequent applications. We consider the HSI classification [6] using the support vector machine (SVM). We use the denoising results of the real-world noisy HSI *Indian* by different methods to conduct the HSI classification. 10% of the samples are set as training set while others are testing set. The results are shown in Fig. 13. We can see that the classification result on the denoising HSI by S2DIP has the best visual quality and accuracy, which verifies the effectiveness and superiority of S2DIP over competing denoising methods.

D. Convergence Analysis

To test the convergence of the ADMM Algorithm 1, we plot the relative error of variables with respect to the iteration number in Fig. 14. The downward trend of the curves verifies the convergence behavior of our method, which favorably addresses the semi-convergence of DIP. This can attribute to the SSTV and the sparse term which respectively considers the HSI spatial-spectral local smoothness and the sparsity of the structural noise. Thus, the proposed model can accurately separate the noise and the clean HSI, resulting in stable convergence.

E. The Generalization of S2DIP

In this subsection, we discuss the generalization of the proposed method. Here, we consider video data⁵ which also contains three-dimensional information. In low light conditions, the videos will be inevitably corrupted by dynamic noise [53], see Fig. 15.

Due to the complexity and irregularity of the real noise, video denoising is extremely challenging. For the heavily corrupted video frames, we use DIP and our method for its restoration. Fig. 15 displays the denoising results, where S2DIP reasonably recovers the clean video and preserves the temporal fidelity. The results of DIP methods, which are manually selected due to the semi-convergence, remain notable noise. The above results illustrate the generalization of S2DIP to handle different types of data and various noise.

VI. CONCLUSION

In this paper, we propose the S2DIP for hyperspectral mixed noise removal. The SSTV regularization is considered to fully explore the HSI spatial-spectral local smooth prior to improve the effectiveness of the unsupervised DIP. The ℓ_1 -norm sparse term is considered to remove the sparse noise. To address the proposed model, we develop an ADMM algorithm. Experimental results on synthetic data and real data demonstrate the effectiveness of the proposed method, which outperforms state-of-the-art methods. Meanwhile, the proposed method favorably alleviates the semi-convergence problem, which always exists in the DIP framework. Our future work would contain the usage of unsupervised CNN and its combination

⁵The real noisy video is captured by our personal device under extremely low light conditions.

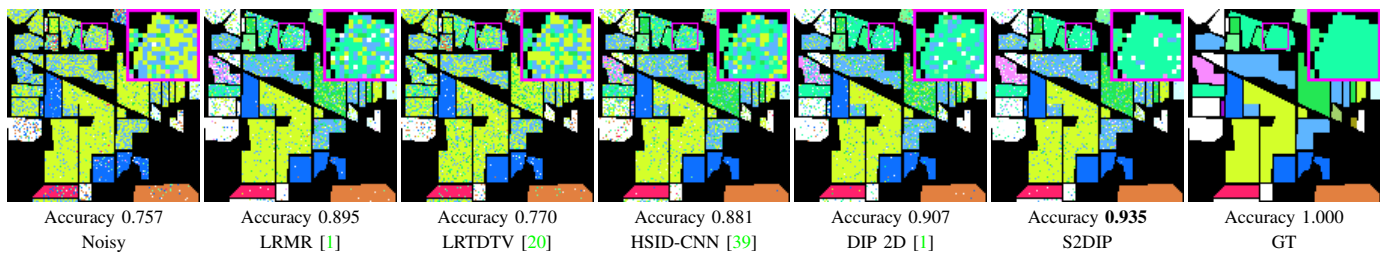


Fig. 13. The HSI classification results using SVM on the denoising results by different denoising methods. Different colors refer to different classifications. The **best** accuracy rate is highlighted by **boldface**.

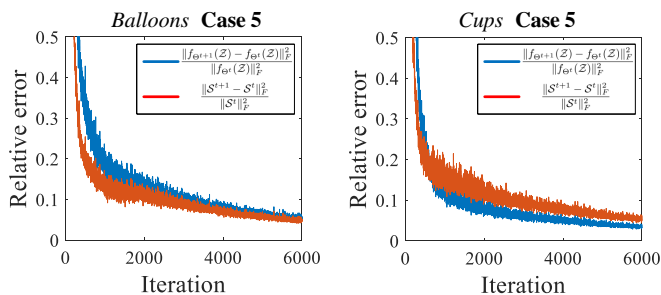


Fig. 14. The relative error of variables with respect to iteration.

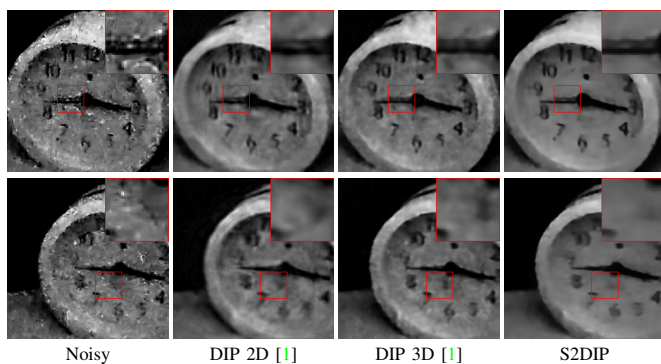


Fig. 15. Two denoising video frames by different methods.

with model-based methods for more applications, especially for multi-dimensional image processing.

REFERENCES

- [1] O. Sidorov and J. Y. Hardeberg, "Deep hyperspectral prior: Single-image denoising, inpainting, super-resolution," in *2019 IEEE/CVF International Conference on Computer Vision Workshop (ICCVW)*, 2019, pp. 3844–3851.
- [2] G. Wang, Y. Zhang, B. He, and K. T. Chong, "A framework of target detection in hyperspectral imagery based on blind source extraction," *IEEE Journal of Selected Topics in Applied Earth Observations and Remote Sensing*, vol. 9, no. 2, pp. 835–844, 2016.
- [3] Y. Liu, G. Gao, and Y. Gu, "Tensor matched subspace detector for hyperspectral target detection," *IEEE Transactions on Geoscience and Remote Sensing*, vol. 55, no. 4, pp. 1967–1974, 2017.
- [4] S. Jia, L. Shen, J. Zhu, and Q. Li, "A 3-D gabor phase-based coding and matching framework for hyperspectral imagery classification," *IEEE Transactions on Cybernetics*, vol. 48, no. 4, pp. 1176–1188, 2018.
- [5] N. Akhtar and A. Mian, "Nonparametric coupled bayesian dictionary and classifier learning for hyperspectral classification," *IEEE Transactions on Neural Networks and Learning Systems*, vol. 29, no. 9, pp. 4038–4050, 2018.
- [6] X. Cao, J. Yao, Z. Xu, and D. Meng, "Hyperspectral image classification with convolutional neural network and active learning," *IEEE Transactions on Geoscience and Remote Sensing*, vol. 58, no. 7, pp. 4604–4616, 2020.
- [7] Y. Wang, L. Lin, Q. Zhao, T. Yue, D. Meng, and Y. Leung, "Compressive sensing of hyperspectral images via joint tensor tucker decomposition and weighted total variation regularization," *IEEE Geoscience and Remote Sensing Letters*, vol. 14, no. 12, pp. 2457–2461, 2017.
- [8] W. He, H. Zhang, and L. Zhang, "Total variation regularized reweighted sparse nonnegative matrix factorization for hyperspectral unmixing," *IEEE Transactions on Geoscience and Remote Sensing*, vol. 55, no. 7, pp. 3909–3921, 2017.
- [9] J. Yao, D. Hong, L. Xu, D. Meng, J. Chanussot, and Z. Xu, "Sparsity-enhanced convolutional decomposition: A novel tensor-based paradigm for blind hyperspectral unmixing," *IEEE Transactions on Geoscience and Remote Sensing*, pp. 1–14, 2021.
- [10] K. Wang, Y. Wang, X.-L. Zhao, J. C.-W. Chan, Z. Xu, and D. Meng, "Hyperspectral and multispectral image fusion via nonlocal low-rank tensor decomposition and spectral unmixing," *IEEE Transactions on Geoscience and Remote Sensing*, vol. 58, no. 11, pp. 7654–7671, 2020.
- [11] W. He, H. Zhang, H. Shen, and L. Zhang, "Hyperspectral image denoising using local low-rank matrix recovery and global spatial-spectral total variation," *IEEE Journal of Selected Topics in Applied Earth Observations and Remote Sensing*, vol. 11, no. 3, pp. 713–729, 2018.
- [12] H. K. Aggarwal and A. Majumdar, "Hyperspectral image denoising using spatio-spectral total variation," *IEEE Geoscience and Remote Sensing Letters*, vol. 13, no. 3, pp. 442–446, 2016.
- [13] S. Takeyama, S. Ono, and I. Kumazawa, "Mixed noise removal for hyperspectral images using hybrid spatio-spectral total variation," in *2019 IEEE International Conference on Image Processing (ICIP)*, 2019, pp. 3128–3132.
- [14] J. Liu, Y. Sun, X. Xu, and U. S. Kamilov, "Image restoration using total variation regularized deep image prior," in *ICASSP 2019 - 2019 IEEE International Conference on Acoustics, Speech and Signal Processing (ICASSP)*, 2019, pp. 7715–7719.
- [15] J. Mairal, F. Bach, J. Ponce, G. Sapiro, and A. Zisserman, "Non-local sparse models for image restoration," in *2009 IEEE 12th International Conference on Computer Vision*, 2009, pp. 2272–2279.
- [16] W. Dong, L. Zhang, G. Shi, and X. Li, "Nonlocally centralized sparse representation for image restoration," *IEEE Transactions on Image Processing*, vol. 22, no. 4, pp. 1620–1630, 2013.
- [17] M. Maggioni, V. Katkovnik, K. Egiazarian, and A. Foi, "Nonlocal transform-domain filter for volumetric data denoising and reconstruction," *IEEE Transactions on Image Processing*, vol. 22, no. 1, pp. 119–133, 2013.
- [18] H. Zhang, W. He, L. Zhang, H. Shen, and Q. Yuan, "Hyperspectral image restoration using low-rank matrix recovery," *IEEE Transactions on Geoscience and Remote Sensing*, vol. 52, no. 8, pp. 4729–4743, 2014.
- [19] W. He, H. Zhang, L. Zhang, and H. Shen, "Total-variation-regularized low-rank matrix factorization for hyperspectral image restoration," *IEEE Transactions on Geoscience and Remote Sensing*, vol. 54, no. 1, pp. 178–188, 2016.
- [20] Y. Wang, J. Peng, Q. Zhao, Y. Leung, X. Zhao, and D. Meng, "Hyperspectral image restoration via total variation regularized low-rank tensor decomposition," *IEEE Journal of Selected Topics in Applied Earth Observations and Remote Sensing*, vol. 11, no. 4, pp. 1227–1243, 2018.
- [21] Y. Chang, L. Yan, and S. Zhong, "Hyper-laplacian regularized unidirectional low-rank tensor recovery for multispectral image denoising," in *2017 IEEE Conference on Computer Vision and Pattern Recognition (CVPR)*, 2017, pp. 5901–5909.
- [22] A. Karami, M. Yazdi, and A. Zolghadre Asli, "Noise reduction of hyperspectral images using kernel non-negative Tucker decomposition," *IEEE Journal of Selected Topics in Signal Processing*, vol. 5, no. 3, pp. 487–493, 2011.
- [23] Q. Xie, Q. Zhao, D. Meng, and Z. Xu, "Kronecker-basis-representation based tensor sparsity and its applications to tensor recovery," *IEEE*

- Transactions on Pattern Analysis and Machine Intelligence*, vol. 40, no. 8, pp. 1888–1902, 2018.
- [24] X. Chen, Z. Han, Y. Wang, Q. Zhao, D. Meng, L. Lin, and Y. Tang, “A generalized model for robust tensor factorization with noise modeling by mixture of gaussians,” *IEEE Transactions on Neural Networks and Learning Systems*, vol. 29, no. 11, pp. 5380–5393, 2018.
- [25] X. Gong, W. Chen, and J. Chen, “A low-rank tensor dictionary learning method for hyperspectral image denoising,” *IEEE Transactions on Signal Processing*, vol. 68, pp. 1168–1180, 2020.
- [26] Y. Peng, D. Meng, Z. Xu, C. Gao, Y. Yang, and B. Zhang, “Decomposable nonlocal tensor dictionary learning for multispectral image denoising,” in *2014 IEEE Conference on Computer Vision and Pattern Recognition*, 2014, pp. 2949–2956.
- [27] W. He, H. Zhang, H. Shen, and L. Zhang, “Hyperspectral image denoising using local low-rank matrix recovery and global spatial-spectral total variation,” *IEEE Journal of Selected Topics in Applied Earth Observations and Remote Sensing*, vol. 11, no. 3, pp. 713–729, 2018.
- [28] L. Zhuang, X. Fu, M. K. Ng, and J. M. Bioucas-Dias, “Hyperspectral image denoising based on global and nonlocal low-rank factorizations,” *IEEE Transactions on Geoscience and Remote Sensing*, pp. 1–17, 2021.
- [29] L. Zhuang, L. Gao, B. Zhang, X. Fu, and J. M. Bioucas-Dias, “Hyperspectral image denoising and anomaly detection based on low-rank and sparse representations,” *IEEE Transactions on Geoscience and Remote Sensing*, pp. 1–17, 2020.
- [30] W. He, H. Zhang, H. Shen, and L. Zhang, “Hyperspectral image denoising using local low-rank matrix recovery and global spatial-spectral total variation,” *IEEE Journal of Selected Topics in Applied Earth Observations and Remote Sensing*, vol. 11, no. 3, pp. 713–729, 2018.
- [31] W. He, H. Zhang, L. Zhang, and H. Shen, “Total-variation-regularized low-rank matrix factorization for hyperspectral image restoration,” *IEEE Transactions on Geoscience and Remote Sensing*, vol. 54, no. 1, pp. 178–188, 2016.
- [32] K. H. Jin, M. T. McCann, E. Froustey, and M. Unser, “Deep convolutional neural network for inverse problems in imaging,” *IEEE Transactions on Image Processing*, vol. 26, no. 9, pp. 4509–4522, 2017.
- [33] X. Mao, C. Shen, and Y.-B. Yang, “Image restoration using very deep convolutional encoder-decoder networks with symmetric skip connections,” in *Advances in Neural Information Processing Systems 29*, 2016, pp. 2802–2810.
- [34] K. He, X. Zhang, S. Ren, and J. Sun, “Deep residual learning for image recognition,” in *2016 IEEE Conference on Computer Vision and Pattern Recognition (CVPR)*, 2016, pp. 770–778.
- [35] R. Dian, S. Li, A. Guo, and L. Fang, “Deep hyperspectral image sharpening,” *IEEE Transactions on Neural Networks and Learning Systems*, vol. 29, no. 11, pp. 5345–5355, 2018.
- [36] P. Zhong and R. Wang, “Jointly learning the hybrid CRF and MLR model for simultaneous denoising and classification of hyperspectral imagery,” *IEEE Transactions on Neural Networks and Learning Systems*, vol. 25, no. 7, pp. 1319–1334, 2014.
- [37] W. Dong, H. Wang, F. Wu, G. Shi, and X. Li, “Deep spatial-spectral representation learning for hyperspectral image denoising,” *IEEE Transactions on Computational Imaging*, vol. 5, no. 4, pp. 635–648, 2019.
- [38] Y. Chang, L. Yan, H. Fang, S. Zhong, and W. Liao, “HSI-DeNet: Hyperspectral image restoration via convolutional neural network,” *IEEE Transactions on Geoscience and Remote Sensing*, vol. 57, no. 2, pp. 667–682, 2019.
- [39] Q. Yuan, Q. Zhang, J. Li, H. Shen, and L. Zhang, “Hyperspectral image denoising employing a spatial-spectral deep residual convolutional neural network,” *IEEE Transactions on Geoscience and Remote Sensing*, vol. 57, no. 2, pp. 1205–1218, 2019.
- [40] Y. Chang, M. Chen, L. Yan, X.-L. Zhao, Y. Li, and S. Zhong, “Toward universal stripe removal via wavelet-based deep convolutional neural network,” *IEEE Transactions on Geoscience and Remote Sensing*, vol. PP, pp. 1–18, 12 2019.
- [41] K. Wei, Y. Fu, and H. Huang, “3-D quasi-recurrent neural network for hyperspectral image denoising,” *IEEE Transactions on Neural Networks and Learning Systems*, pp. 1–13, 2020.
- [42] V. Lempitsky, A. Vedaldi, and D. Ulyanov, “Deep image prior,” in *2018 IEEE/CVF Conference on Computer Vision and Pattern Recognition*, 2018, pp. 9446–9454.
- [43] Q. Yuan, L. Zhang, and H. Shen, “Hyperspectral image denoising employing a spectral-spatial adaptive total variation model,” *IEEE Transactions on Geoscience and Remote Sensing*, vol. 50, no. 10, pp. 3660–3677, 2012.
- [44] W. He, N. Yokoya, L. Yuan, and Q. Zhao, “Remote sensing image reconstruction using tensor ring completion and total variation,” *IEEE Transactions on Geoscience and Remote Sensing*, vol. 57, no. 11, pp. 8998–9009, 2019.
- [45] H. Zhang, L. Liu, W. He, and L. Zhang, “Hyperspectral image denoising with total variation regularization and nonlocal low-rank tensor decomposition,” *IEEE Transactions on Geoscience and Remote Sensing*, vol. 58, no. 5, pp. 3071–3084, 2020.
- [46] H. Zhang, J. Cai, W. He, H. Shen, and L. Zhang, “Double low-rank matrix decomposition for hyperspectral image denoising and destriping,” *IEEE Transactions on Geoscience and Remote Sensing*, pp. 1–19, 2021.
- [47] Q. Zhang, Q. Yuan, J. Li, X. Liu, H. Shen, and L. Zhang, “Hybrid noise removal in hyperspectral imagery with a spatial-spectral gradient network,” *IEEE Transactions on Geoscience and Remote Sensing*, vol. 57, no. 10, pp. 7317–7329, 2019.
- [48] X. Cao, X. Fu, C. Xu, and D. Meng, “Deep spatial-spectral global reasoning network for hyperspectral image denoising,” *IEEE Transactions on Geoscience and Remote Sensing*, pp. 1–14, 2021.
- [49] Z. Qiu, T. Yao, and T. Mei, “Learning spatio-temporal representation with pseudo-3d residual networks,” in *2017 IEEE International Conference on Computer Vision (ICCV)*, 2017, pp. 5534–5542.
- [50] D. Kingma and J. Ba, “ADAM: A method for stochastic optimization,” *International Conference on Learning Representations*, 12 2014.
- [51] F. Yasuma, T. Mitsunaga, D. Iso, and S. K. Nayar, “Generalized assorted pixel camera: Postcapture control of resolution, dynamic range, and spectrum,” *IEEE Transactions on Image Processing*, vol. 19, no. 9, pp. 2241–2253, 2010.
- [52] B. R. Shivakumar and S. V. Rajashekaradhy, “Performance evaluation of spectral angle mapper and spectral correlation mapper classifiers over multiple remote sensor data,” in *2017 Second International Conference on Electrical, Computer and Communication Technologies (ICECCT)*, 2017, pp. 1–6.
- [53] W. Wang, X. Chen, C. Yang, X. Li, X. Hu, and T. Yue, “Enhancing low light videos by exploring high sensitivity camera noise,” in *2019 IEEE/CVF International Conference on Computer Vision (ICCV)*, 2019, pp. 4110–4118.